PAPER

Supersonic jet interactions with a micro-engineered skimmer

IOP Publishing Journal of Micromechanics and Microengineering
J. Micromech. Microeng. **28** (2018) 085017 (13pp) https://doi.org/10.1088/1361-6439/aac001

Supersonic jet interactions with a micro-engineered skimmer

S Wright[1] **and R R A Syms**[2]

[1] Microsaic Systems, GMS House, Boundary Road, Woking, Surrey, GU21 5BX, United Kingdom
[2] EEE Department, Imperial College London, Exhibition Road, London, SW7 2AZ, United Kingdom

E-mail: r.syms@imperial.ac.uk

Received 14 December 2017, revised 8 March 2018
Accepted for publication 25 April 2018
Published 15 May 2018

Abstract

A micro-engineered, skimmer-based vacuum interface has been demonstrated and used to investigate gas dynamics on a sub-millimeter length scale. The interface is fabricated as a stacked assembly of silicon dies, based on an anisotropically etched inlet orifice and a pyramidal skimmer cone formed in electroplated nickel. Expansion of gas into vacuum, interaction of a supersonic jet with the skimmer and transmission of a collimated beam into a second vacuum stage have all been imaged with a schlieren microscope. Using a glass-walled vacuum chamber, flow patterns upstream and fully downstream of the skimmer have been imaged together for the first time. At low first-stage pressures, the 150–200 μm tall skimmers cannot fully penetrate the shock arising from interaction of the jet with the back wall. However, as the pressure is increased, a multiple shock cell structure evolves, the jet narrows and transmission rises sharply. Eventually, a collimated beam is transmitted to the second stage. When the skimmer aperture is smaller than the source aperture, a series of distinct peaks is evident in a plot of transmission against first-stage pressure. Imaging shows that at each successive peak, the number of shock cells increases by one and the skimmer inlet is coincident with a node.

Keywords: vacuum interface, skimmer, schlieren imaging, micro-jet, bulk micromachining

(Some figures may appear in colour only in the online journal)

1. Introduction

Conical skimmers are widely used to extract intense, well-collimated molecular beams from supersonic gas expansions [1, 2]. While early development was driven by the need for high-intensity sources in the field of chemical reaction dynamics [3], many other applications have since emerged. However, the most important application is in mass spectrometry, where skimmer-based interfaces are used to transfer gas and entrained ions from atmospheric pressure ionisation sources to mass analysers in high vacuum [4–6]. In this paper, we describe the development of a microelectromechanical systems (MEMS) skimmer-based interface for use in miniature mass spectrometers [7–9]. There has been considerable progress in MEMS mass spectrometry [10], but this key component has received remarkably little attention. Here we present a first design for a MEMS-based skimmed free-jet vacuum interface and the results of fabrication and initial characterisation. Imaging of supersonic gas flows within a MEMS assembly, which has not previously been attempted, is an important achievement of this work.

Relevant aspects of macroscopic and microscopic supersonic expansions are first reviewed in section 2, and an overview of the MEMS-based vacuum interface is presented. Details of device fabrication, optical imaging, operation in vacuum and coupling to mass spectrometry are given in section 3. Experimental results are described and discussed in section 4, and conclusions are drawn in section 5.

2. Macroscopic and microscopic supersonic expansions

In this Section, aspects of supersonic gas dynamics relevant to skimmer operation are reviewed. An overview of the proposed MEMS vacuum interface is given, and contrasted with previous work on miniature jets, nozzles and skimmers.

2.1. Macroscopic free jet expansion

The dynamics of jet formation when gas passes from a high-pressure source to a low-pressure region via an orifice or shaped nozzle and the subsequent interaction of the flow with a skimmer are well understood [1, 2, 5, 11–13]. The flow is compressible and may be interpreted in terms of isentropic transitions, which describe the relationships between jet pressure, temperature, density and speed under the assumption that all processes are adiabatic and the viscosity is zero i.e. there are no frictional interactions with the nozzle walls or background gas in the low pressure region. In a convergent nozzle, or when streamlines compress to pass through an orifice, an initial acceleration occurs as the flow cross-section decreases. The stream velocity during this initial acceleration is limited to $M = 1$, where M is the local Mach number. This occurs at the sonic plane, which is generally assumed to coincide with the nozzle throat or the orifice plane. Further increases in velocity to $M > 1$ can only be achieved by allowing the gas to expand into a low-pressure region downstream of the sonic plane.

In convergent-divergent nozzles, such as those used in rocket engines, the divergent section controls the expansion such that, ideally, there is no further expansion or compression of the flow as it leaves the nozzle. However, in laboratory molecular beam systems and vacuum interfaces, the divergent section is often omitted to avoid viscous interactions between the jet and the walls. Consequently, the gas expands as a free jet. In the early stages of the expansion, collisions between molecules result in the enthalpy of the reservoir gas being converted into the kinetic energy of the directed mass flow. Hence, the rotational and vibrational quantum state populations and the radial velocity distribution are all cooled while the stream velocity increases. Trading of thermal energy for directed acceleration results in an improvement in centreline flux (compared to an effusive source) that scales as $(\gamma/2)M^2$, where $\gamma = C_P/C_V$ is the ratio of heat capacities C_P and C_V at constant pressure and constant volume [14]. Jet cooling leads to applications in cluster beams and high-resolution spectroscopy, while flow directionality allows efficient transfer of ions in mass spectrometers.

If the downstream pressure, P_1, is lower than about 10^{-2} mbar, the free jet is diffuse, but at higher pressures the jet is bounded by shocks, namely the barrel shock and the Mach disc shown in figure 1(a). The latter is approximately perpendicular to the beam axis and consequently referred to as a normal shock. These shock structures are a consequence of transitions from free jet conditions to background isotropic gas conditions and are characterised by abrupt changes in density, temperature, pressure, and entropy. In the region enclosed by the barrel shock and Mach disc, the so-called 'zone of silence', the flow is almost collision-free and characterised by straight streamlines and high Mach numbers.

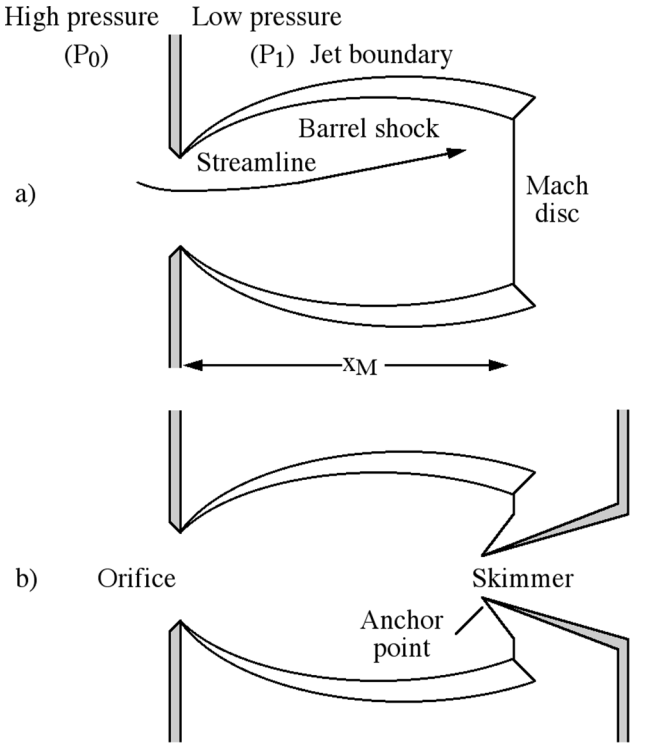

Figure 1. (a) Structure of a supersonic free jet expansion. (b) Shock attachment to an ideal skimmer. Reprinted with permission from [2]. Copyright (1984) American Chemical Society. Reprinted from [15], Copyright (1966), with permission from Academic Press.

A molecular beam can be transmitted to a second vacuum stage by allowing a skimmer to sample the flow from the core of the expansion. In the low-pressure regime ($P_1 < 10^{-2}$ mbar), the design and positioning of the skimmer are not critical. However, at higher pressures ($P_1 > 10^{-2}$ mbar), the skimmer must be positioned to pierce the Mach disc and designed with a profile that allows an oblique shock to attach to the skimmer as shown in figure 1(b). If the skimmer is blunt or has a sub-optimal profile, a bow shock appears in front of the tip, which re-heats and scatters the gas flow. As skimmer design and positioning for high-pressure operation were not initially understood, early molecular beam instruments operated in the low pressure regime, which required high capacity pumps. However, Campargue later showed [2] that sharp, conical skimmers with an internal angle of 45° and an external angle of 55° are capable of shock-free sampling from the zone of silence, allowing skimmers to be operated using much smaller pumps. Campargue used a 19 mm tall skimmer with a 500 μm diameter aperture, which was separated by a distance of 20 mm from a 30 μm diameter inlet nozzle.

2.2. MEMS-based skimmed free jet expansion system

Conventionally, skimmers are fabricated by machining or electroplating on the outside of a tapered mandrel [16, 17]. Here, we describe jet interactions in microfabricated skimmer systems with significantly reduced size (150–200 μm tall,

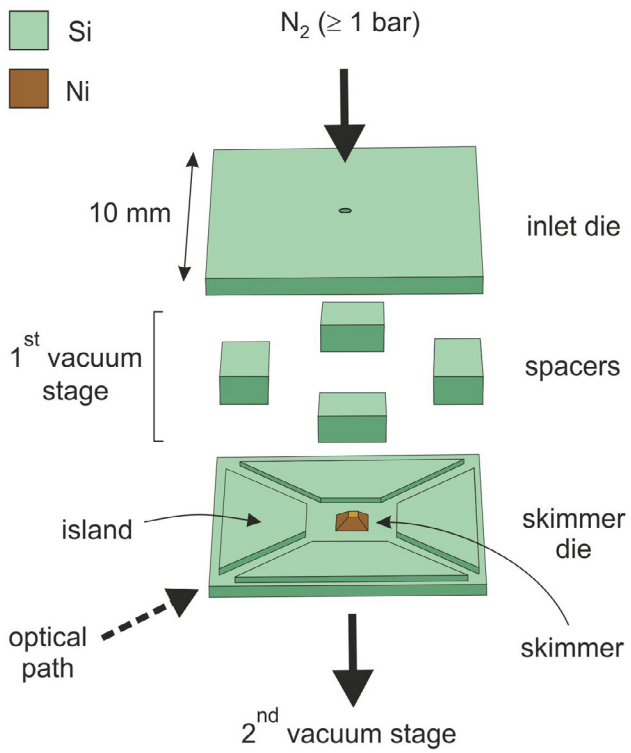

Figure 2. Exploded view of the skimmer assembly. The spacers are 800 μm deep. For clarity, the skimmer has been drawn on an exaggerated scale. Nitrogen passes through the inlet capillary and expands into the first vacuum stage. The resulting supersonic jet interacts with the skimmer and a portion is transmitted into the second vacuum stage.

with 50–100 μm apertures). The skimmers are fabricated as thin-walled, truncated square pyramids, formed by electroplating on the inside of an etched mould. Although unusual, pyramidal skimmers with rectangular apertures have been used for curtain beam applications [18–20]. The inlet is a 100 μm diameter, 400 μm long capillary whose output is separated from the skimmer by a distance of 800 μm. Schlieren imaging and gas throughput measurements are used to characterise the interactions of the jet with the skimmer and transmission into a second vacuum stage over a wide pressure range ($P_1 = 5$–500 mbar).

Figure 2 shows an exploded view of the skimmer assembly. The components were fabricated using silicon MEMS processing. In contrast to molecular beam systems employing alignment stages to optimise nozzle position [21], the assembly is pre-aligned during fabrication and permanently bonded to yield a compact ($10 \times 10 \times 1.7$ mm) monolithic device. Nitrogen gas from a reservoir at $P_0 = 1$–3 bar expands from an inlet capillary etched through the upper silicon die. The skimmer is formed in electroplated nickel [22, 23] and supported on the lower silicon die. The walls are 10 μm thick and inclined at 54.7° to the horizontal. This angle is dictated by the crystal planes of silicon and cannot be varied. However, it fortuitously matches the optimum value determined by Campargue [2]. Raised islands protect the skimmer from damage during processing and assembly. Spacers maintain a separation of 800 μm between the dies and provide passages for pumping and imaging.

2.3. Previous work on MEMS nozzles and micro-jets and miniature skimmers

There has been considerable interest in micro-scale gas expansions in connection with propulsion systems. Numerous nozzle-based MEMS micro-thrusters have been developed for micro-satellite attitude adjustment. For example, square-section silicon nozzles have been fabricated by through-wafer anisotropic etching [24, 25] and 2D nozzles with vertical walls have been formed by anisotropic plasma etching [26–31]. MEMS nozzles are often fabricated as multilayer stacks [24, 25, 30, 32]. As the size scale is reduced, viscous interactions with the walls become increasingly important [31, 33].

The structure of micro-jets emanating from nozzles and capillary tubes has been examined using schlieren and shadowgraph imaging to probe density variations, and Pitot tube measurements to interrogate pressure distributions [34–39]. For jets expanding at atmospheric pressure, extended multiple shock cell structures have been observed. Imaging of micro-jets impinging on flat plates and sharp needles has also been reported [35, 38]. Although there are some departures from expected behaviour for very small nozzles [36], investigations have shown that micro-jets mainly behave in the same way as large jets, with characteristics that can simply be scaled according to the nozzle diameter.

A micro-jet exhausting into vacuum, rather than ambient conditions, has also been investigated using the schlieren technique [40]. A 2D Laval nozzle with a 250 μm throat was used and a jet extending over several millimetres was imaged. Due to the low density gradients involved, the shock structure was only evident when the image was displayed as a ratio of the jet image to a background reference image. The schlieren imaging undertaken here is more difficult because of the smaller jet dimensions and the location of the jet within a monolithic assembly.

Glass micropipettes with 3–10 μm diameter apertures have previously been used as miniature skimmers [21, 41]. However, they were mounted on conical supports that positioned the skimmer tip well away from the back wall. In effect, these are conventionally sized skimmers with unusually small apertures. Moreover, the first vacuum stage was pumped with high vacuum pumps to 10^{-4} mbar, allowing operation in the low-pressure regime.

3. Experimental details

In this Section, we present further details of fabrication, and the main assessment methods used: schlieren imaging, operation in vacuum and coupling to mass spectrometry.

3.1. Skimmer fabrication

Fabrication is based on the use of anisotropic crystal plane etching to form pyramidal holes in a (1 0 0) Si wafer [42, 43]. A thin seed layer of nickel is deposited on the sidewalls and thickened by electroplating. Proud, free-standing skimmers are then revealed by removal of the silicon electroplating mould from the reverse side of the wafer by deep reactive

ion etching (DRIE) [44, 45]. The process flow is described in more detail below with reference to figure 3.

The starting material was a 100 mm diameter, 0.525 mm thick, (1 0 0) Si wafer carrying 200 nm of Si_3N_4 deposited by low-pressure chemical vapour deposition. Using a first mask, the Si_3N_4 layer was patterned by mid-UV photolithography and reactive ion etching in a mixture of CHF_3, O_2 and Ar gas, using an Oxford Instruments PlasmaLab 80^+. Exposed silicon was then etched in KOH, yielding blind, pyramidal holes in the substrate as a result of differing etch rates between the (1 0 0) and (1 1 1) crystal planes (steps 2–3). The relationship between the width of the square mask opening W_B, the etch depth D and the width W_A at the bottom of the blind pyramidal hole thus formed can be found from the crystal plane angle $\theta = \cos^{-1}(1/\sqrt{3}) = 54.7°$ and simple trigonometry, as $W_B = W_A + D\sqrt{2}$. Assuming that $D = 500$ μm and $W_A = 50$ mm, we obtain $W_B = 757$ μm. A larger value of W_A (say, 100 μm) may then be obtained simply by etching to a smaller depth D. IPA was added to the etchant, to control micro-pyramid formation.

During initial development, the process flow continued with deposition of nickel followed by plasma etching of silicon from the reverse of the wafer and wet etching to open the skimmer aperture. However, electrochemical issues during wet etching resulted in low yield. Consequently, the alternative strategy shown in figure 3, which uses plasma etching steps, was adopted. After stripping the remaining Si_3N_4, a Cr layer was deposited on the reverse side of the wafer by sputtering, and then patterned using a second mask to define the islands, channels and cleaving lanes (steps 4–7). Partial removal of the bulk silicon by DRIE in an STS Single Chamber Multiplex inductively-coupled plasma etcher then exposed square apertures defined by the pyramidal holes (step 8). After deposition of a Cr/Ni seed layer in a Nordiko RF sputter coater, additional Ni was deposited by electroplating. Free-standing skimmers with inherently open apertures were then revealed by deep reactive ion etching additional silicon from the reverse side (steps 9–10). Finally, dies were separated by cleaving. Figure 4 shows a scanning electron microscope (SEM) image of a completed skimmer die, together with a close-up view of the skimmer cone. Skimmers with 100×100 μm and 50×50 μm apertures were fabricated. After extensive use, one of the nominally 50×50 μm apertures measured 65×65 μm. However, the skimmer sidewalls were also eroded, presumably due to high velocity particulates in the unfiltered nitrogen feed gas, which may have led to some widening of the aperture.

Fabrication of the silicon dies carrying inlet capillaries was much simpler, requiring only patterning of a thick resist followed by DRIE. Complete vacuum interfaces were assembled as a stack, using an optical microscope to monitor alignment by alternately focusing on the front face of the inlet aperture and then through the capillary to the skimmer aperture, which was backlit with an LED. The stack was manipulated until the relative alignment was better than 10 μm and then secured by applying a bead of adhesive across the three layers at each spacer position. The ability to co-integrate structural parts in the Si substrate can be exploited to add mechanical

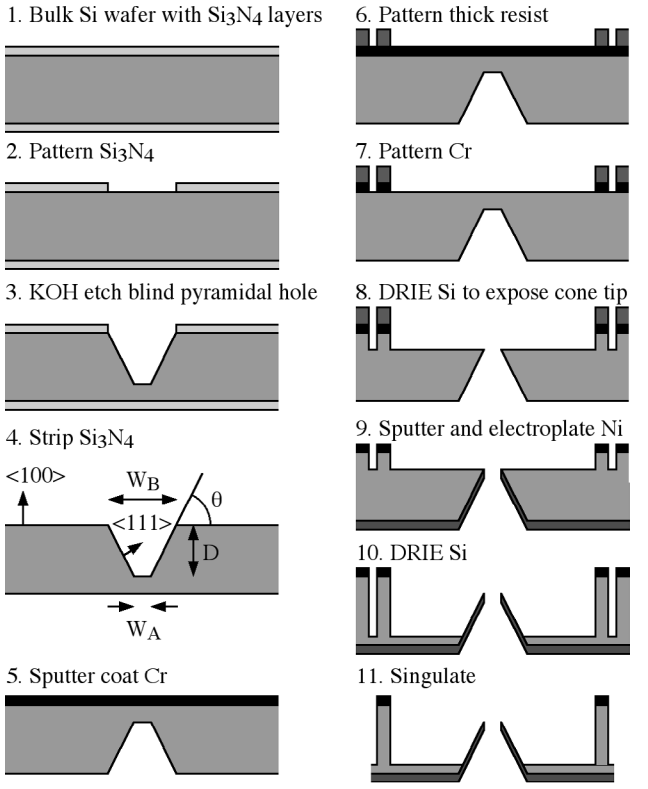

Figure 3. Skimmer microfabrication process. Pyramidal holes were produced in a (1 0 0) silicon wafer by anisotropic crystal etching (steps 1–8). After sputter deposition of nickel on the internal walls (step 9), excess Si was removed from the reverse side of the wafer (step 10), leaving free-standing Ni skimmers supported on a Si substrate.

alignment features, which will allow the passive self-alignment methods already used to assemble mass filters [10]. Using a mask aligner with double-sided alignment optics rather than through-wafer imaging, an accuracy of <2 μm is to be expected. Such methods will be explored in future iterations.

3.2. Schlieren imaging and vacuum systems

A schlieren microscope was developed to image sub-millimeter gas jets under vacuum conditions. Figure 5 shows a schematic representation of the system. Light from a 1 mm diameter pinhole source was collimated by a plano-convex lens, L1. A vacuum bench housing the MEMS vacuum interface was positioned between L1 and a second lens, L2, which were 25 cm apart. Plano-convex lenses L2 and L3 formed a beam expander whose magnification is given by the ratio of the focal lengths. For L2, f = 30 mm, and for L3, f = 150 or 250 mm, resulting in magnifications of $\times 5$ and $\times 8$, respectively. Images were recorded by a CCD colour video camera (JVC TK-1280E). A knife-edge on an *x*-*y* stage was moved into the beam path at the common focal point of L2 and L3 to attenuate the light intensity by approximately 50%. In schlieren imaging, gas density gradients within the interaction region cause light rays to be refracted away from parallel. These rays are not focussed at the knife-edge and are consequently not attenuated to the same extent as parallel rays. The

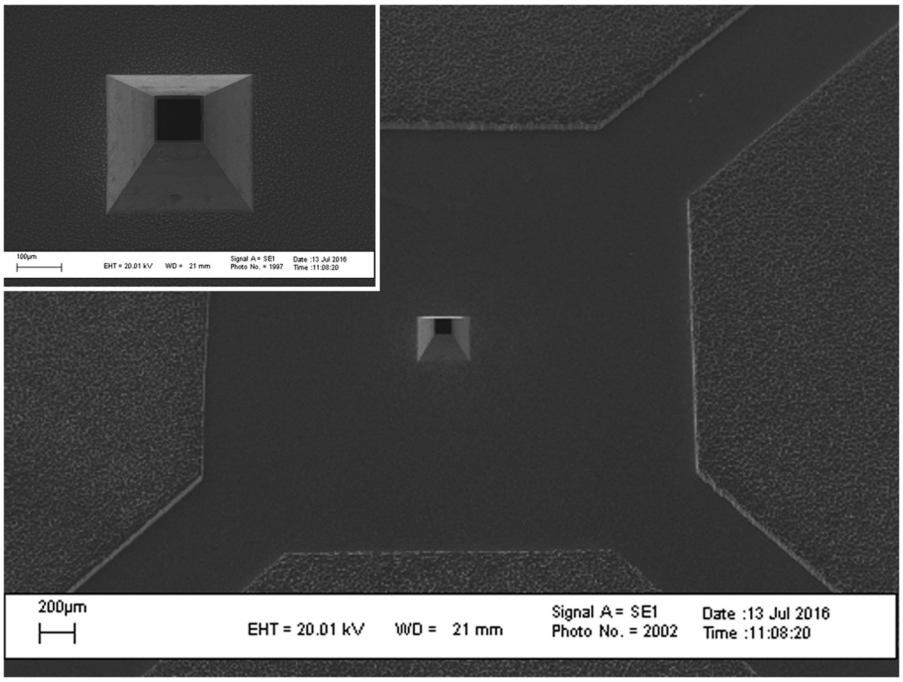

Figure 4. SEM images of a microfabricated Ni skimmer with a 100 × 100 μm aperture.

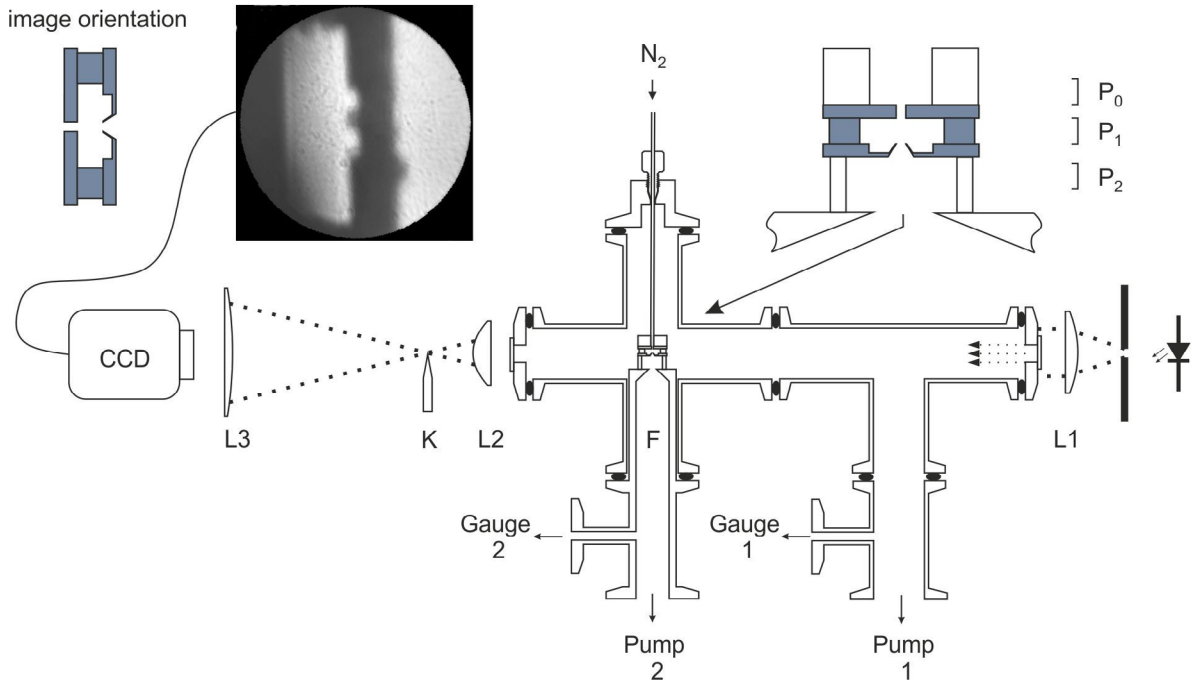

Figure 5. Vacuum and schlieren imaging systems. Collimated light from a pinhole source passes through a two-stage vacuum bench. The skimmer assembly is mounted on a vacuum finger, F. Regions upstream and downstream of the skimmer are illuminated. The image is magnified by lenses L2 and L3. A knife edge, K, at the common focus of L2 and L3 partially blocks the light beam and generates a schlieren image.

flow patterns associated with gas expansion into vacuum are therefore revealed as regions that are lighter or darker than the background.

The vacuum bench was constructed from a standard vacuum tee and a 4-way cross with KF25 flanges. Internal surfaces were blackened to minimise stray light. The collimated light beam entered through a first window, passed through the skimmer assembly, and exited through a second window. The skimmer assembly was mounted on a tubular vacuum finger, F, that provided downstream pumping. In some experiments, the skimmer assembly was bonded directly on to the vacuum finger, while in others, an 8 × 8 × 8 mm square-section glass tube fabricated from microscope slides was inserted between the skimmer assembly and the vacuum finger to allow simultaneous imaging of the gas flow upstream and downstream of the skimmer. Nitrogen gas at 1–3 bar was introduced through

a 1/16″ stainless steel tube, which was attached to the silicon inlet die using a brass collar and epoxy adhesive.

A scroll pump (Varian SH-110) throttled by an in-line valve was used to pump the first stage. However, it would be possible to access most of the pressure range of interest with a small diaphragm pump of the type previously used in miniature mass spectrometers [7, 8]. The second stage was pumped by a turbo pump (Pfeiffer HiPace 80), a rotary pump (Leybold Trivac D4B) or a diaphragm pump (KNF Neuberger N84.4ANDC), depending on the size of the skimmer aperture and the desired second stage pressure. To compare skimmer transmission characteristics, second stage pressure measurements were converted to absolute gas flow rates (1013.25 mbar, 273.15 K) using the effective pumping speed for each pump (determined from measurements of the exhaust gas flow at representative pressures).

Initial tests showed that, with the vacuum bench removed, a gas jet expanding into the laboratory from a 0.8 mm diameter pipette tip with P_0 ~ 4 bar could be observed with the naked eye with the schlieren image projected on a white screen. However, the gas flow rate was two orders of magnitude lower for the 100 μm diameter inlet capillaries used in subsequent experiments. Consequently, images were only revealed after extended video integration and background subtraction.

Video was recorded first with the jet present and then at base vacuum with the gas supply off. Frame stacking and background subtraction were performed using Registax 6.1 video processing software [46]. The jet-off video was integrated first and the resulting bitmap used as the dark field background image during integration of the jet-on video. Images of the jet were revealed after gamma correction and basic contrast adjustment in Registax followed by final adjustment of floor and ceiling colour-scale levels using GIMP 2.8 image processing software [47]. The signal-to-noise ratio was improved without loss of resolution by averaging the RGB layers and displaying as a grey-scale image. In some cases, the final image of the flow pattern was superimposed on the background image to show the position of the jet with respect to structural features.

3.3. Mass spectrometry

The ability of the skimmer assembly to transmit ions from an atmospheric pressure ion source was evaluated using a test rig based on a commercial miniature mass spectrometer (MiD4000, Microsaic Systems, Surrey, UK). Ions were created by electrospray ionization of thiabendazole at a concentration of 1 μg ml^{-1} in a 50/50 mixture of water and acetonitrile with 0.1% formic acid. To bias the inlet electrically with respect to the skimmer, a polymer tab was inserted under each spacer block before final assembly. The height of the peak at *m/z* 202 in the mass spectrum, which corresponds to the $(M + H)^+$ ion, was taken as a measure of transmitted ion flux.

4. Results and discussion

In this section, we begin by discussing the nature of the flow through the inlet capillary. Boundary layer and non-ideal effects are evaluated by comparing measured and theoretical flow rates. We then present schlieren images of jets obtained at high pressure ratio, and examine the implications of shock thickening in free jets and interactions of the jet with the skimmer die. Narrowing of the jet at lower pressure ratios and the transmission of a collimated beam to the second stage are then characterised using gas flow measurements and further schlieren imaging. Finally, we demonstrate the use of the MEMS skimmer assembly as a vacuum interface for a mass spectrometer, and link throughput oscillations with the periodic shock cell structure seen in extended supersonic jets.

4.1. Flow through the inlet capillary

As already discussed, when gas passes from a high pressure source to a low pressure sink via a thin orifice or a convergent nozzle, the flow accelerates as the cross-sectional area of the stream decreases, and a maximum velocity of M = 1 can be achieved at the sonic plane. The molecular flow rate, G, through the sonic plane is clearly

$$G = n^* a^* A^* \tag{1}$$

where n^* and a^* are the number density and speed of sound at the sonic plane, respectively, and A^* is the cross-sectional area at which M = 1 is achieved.

For 1D isentropic flow, a number of standard relations allow the state variables and associated properties to be expressed in terms of the Mach number [48–50]. Equations for density, speed of sound, and temperature, which will be used here and in the next section, are listed below:

$$\frac{n}{n_0} = \left\{1 + \frac{(\gamma - 1)\,M^2}{2}\right\}^{1/(1-\gamma)} \tag{2}$$

$$\frac{a}{a_0} = \left\{1 + \frac{(\gamma - 1)\,M^2}{2}\right\}^{-1/2} \tag{3}$$

$$\frac{T}{T_0} = \left\{1 + \frac{(\gamma - 1)\,M^2}{2}\right\}^{-1}. \tag{4}$$

Here, n_0, a_0, and T_0 are the density, speed of sound, and temperature for the stagnant reservoir gas, respectively, while n, a, and T are the corresponding values at Mach number M.

By evaluating equations (2) and (3) at M = 1, n^* and a^* can be expressed in terms of n_0 and a_0, allowing equation (1) to be re-written as

$$G = \left(\frac{2}{\gamma + 1}\right)^{\frac{\gamma+1}{2(\gamma-1)}} n_0 a_0 A^* = 0.455\, n_0 a_0 D^2 \tag{5}$$

where D is the diameter at the sonic plane and $\gamma = 7/5$ for nitrogen. The effective diameter may be less than the optical diameter due to slower moving, subsonic gas in the boundary layer. Equation (5) is often modified by a discharge coefficient, C_D, to account for this reduction in source area [1].

However, the inlet used here is a short capillary rather than a thin orifice. In the extreme case of a long, narrow capillary inlet, isentropic assumptions are no longer valid and flow

should instead be considered as isothermal and irreversible due to viscous interactions with the walls [51–53]. As a result of friction, a higher reservoir pressure is needed to achieve the same throughput as a thin orifice of the same diameter [51]. Although there is some compression of the flow at the entrance, flow acceleration in a long capillary is predominantly caused by the decrease in pressure along its length, with the sonic plane located just inside the exit [51]. Capillary supersonic jet sources with length-to-diameter ratios of $L/D > 100$ are known to exhibit viscous drag [38, 51]. For the short capillaries used here, $L/D = 4$; this value is similar to the length-to-throat diameter ratios of many convergent-divergent nozzles, for which isentropic flow is generally assumed.

When viscous drag is important, the flow rate will be less than the value predicted by equation (5). By measuring the exhaust flow from the first and second stage pumps, we find that the flow through an inlet capillary with a diameter of 105 ± 5 μm is 1.55 ± 0.02 mbar $\cdot$ 1 s^{-1} at an ambient pressure and temperature of 1018 mbar and 294 K, respectively. According to equation (5), the expected flow rate is 1.63 mbar $\cdot$ 1 s^{-1}. The close correspondence between these values indicates that viscous drag is relatively unimportant and an isentropic flow assumption is valid. The small discrepancy can be accommodated by using $C_D = 0.95$.

4.2. Skimmer interactions with the jet at $P_0/P_1 > 40$

Before imaging gas flow inside the skimmer assembly, the characteristics of free micro-jets were examined. For these experiments, the skimmer and vacuum finger were removed, leaving the inlet die supported by a rigid nitrogen supply tube at the centre of the vacuum system. Figure 6 shows a series of schlieren images corresponding to the highest inlet pressure ratios (P_0/P_1) investigated. The nitrogen reservoir pressure was 3 bar. In each case, a barrel shock and a Mach disc, the familiar characteristics of a supersonic free jet expansion, can be seen. The axial density gradient associated with re-compression of the supersonic flow at the Mach shock is visualized as a dark band. In their seminal work, Ashkenas and Sherman [15] showed that the position of the Mach disc, x_M, is related to the nozzle pressure ratio by

$$\frac{x_M}{D} = 0.67\sqrt{\frac{P_0}{P_1}} \tag{6}$$

for $15 < P_0/P_1 < 17000$. The Mach disc in figure 6(d), which was recorded at $P_0/P_1 = 450$, is located at $x_M/D = 14.5 \pm 0.5$. In good agreement, equation (6) predicts $x_M/D = 14.2$ for this pressure ratio.

The free jet expansions in figure 6 resemble images of larger jets [11, 54] except that the shock structures, which usually appear vanishingly thin, are comparatively thick here. Moreover, the thickness increases as P_0/P_1 decreases and the jet shrinks. This suggests that shock thickness does not scale in the same way as the dimensions of the free jet. Normal shock thicknesses in shock tubes, wind tunnels and free jets have been investigated using electron beam attenuation, electron beam and laser-induced fluorescence, Raman spectroscopy,

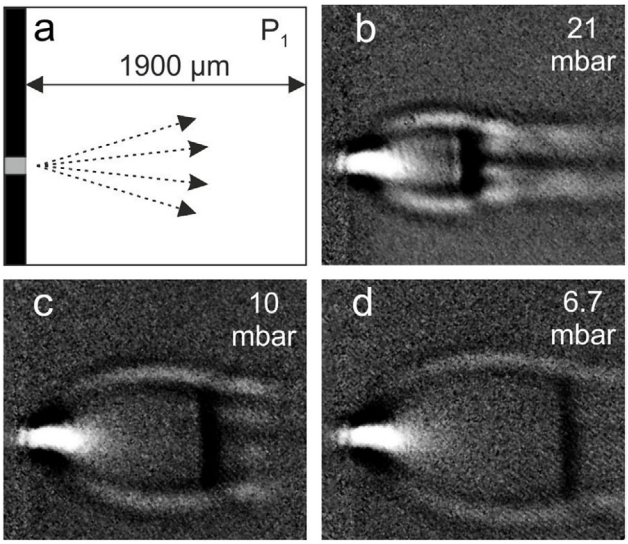

Figure 6. Schlieren images of free jets. The inlet position and scale are indicated in (a) and images corresponding $P_1 = 21$, 10 and 6.7 mbar are shown in (b)–(d). $P_0 = 3$ bar. The Mach disc (dark vertical band) grows thicker as the jet shrinks.

and simulations [13, 55–57]. Typically, shock thicknesses are normalized to the mean free path, λ, since the rapid deceleration in the shock is a consequence of collisions between jet molecules and the background gas. In some reports, the mean free path downstream of the shock is invoked [2] while in others the upstream value is preferred [55–57]. Measurements of nitrogen free jet density profiles by Raman spectroscopy [56, 57] have shown that the thickness of the Mach disc is 4.37 λ for $7.7 \leqslant M \leqslant 15.3$, where λ is evaluated using the spectroscopically determined density and temperature just upstream of the shock, and a soft sphere scattering model.

In the absence of direct measurements, approximate values for the jet density and temperature can be calculated using equations (2) and (4). However, this requires knowledge of the Mach number. According to Ashkenas and Sherman [15], the axial variation in Mach number is given by:

$$M = A\left(\frac{x - x_0}{D}\right)^{\gamma-1} - \frac{\gamma + 1}{2(\gamma - 1)}\left\{A\left(\frac{x - x_0}{D}\right)^{\gamma-1}\right\}^{-1} \tag{7}$$

where $A = 3.65$ and $x_0/D = 0.4$ when $\gamma = 7/5$. Hence, for each of the jets in figures 6(b)–(d), the Mach number, density and temperature can be determined at a position just upstream of the Mach disc. This then allows calculation of λ and the expected shock thickness according to [56, 57]. Measured and expected shock thicknesses are given in table 1. For the $M = 7.7$ jet, the measured thickness is much higher than expected. However, the discrepancy is smaller at $M = 9.4$ and the two values converge at $M = 10.2$.

Shock thickening is a well-known phenomenon [58] and observations of unusually thick Mach discs have been reported previously. Ashkenas and Sherman note that viscous effects cause thickening of the barrel shock and Mach disc [15] while imaging of low density jets by Rothe [59] show exceptionally thick and diffuse Mach discs. In both

Table 1. Measured Mach disc thicknesses ($\delta^{measured}$) for the jets in figures 6(b)–(d) and expected thicknesses ($\delta^{expected}$) based on Raman spectroscopy of larger jets [56, 57]. The error in $\delta^{measured}$ is ± 15 μm.

Jet	x/D	M	$\delta^{expected}$ [μm]	$\delta^{measured}$ [μm]
Figure 6(b)	7.6	7.7	25	140
Figure 6(c)	11.8	9.4	58	120
Figure 6(d)	14.5	10.2	85	80

cases, the shock thickening is linked to low nozzle Reynolds numbers. Reynolds number is defined at the sonic plane as $Re = \rho^* u^* D/\mu^*$, where ρ^*, u^*, and μ^* are the density, speed and viscosity. At high Reynolds numbers, the flow is dominated by inertial forces and expansion is characterized by distinct shock structures. If the Reynolds number is reduced (by decreasing the reservoir pressure and/or employing a narrower source), viscous forces become more important, leading to thicker and more diffuse shocks. Eventually, the shocks disappear altogether [54] and the source becomes essentially effusive. For the jets in figures 6(b) and (c), viscous mixing may be contributing to the thickness of the Mach discs. However, the shock boundaries are surprisingly well-defined, rather than diffuse. Moreover, reducing the reservoir pressure (to lower the Reynolds number) but maintaining the same P_0/P_1 value (to leave the Mach number unchanged) does not lead to additional thickening.

Figure 7 shows schlieren images of jets inside a complete MEMS vacuum interface. Note that the pressure inside the assembly is likely to have been somewhat higher than the value measured in the outer vacuum vessel. The jets no longer have a barrel shape and the vertical Mach disc is replaced by a curved shock comprising of both dark and bright bands. As schlieren imaging is sensitive to density gradients, a dark band followed by a bright band is indicative of a local maximum in the number density profile. Referring back to equation (6), it is clear that as P_1 decreases, the position of the Mach disc is expected to advance across the gap and eventually interact with skimmer, ideally via attachment of an oblique shock to the skimmer rim as shown in figure 1(b). The images in figure 7 show that the Mach disc does indeed move downstream and that tails extending from the barrel shock initially straddle the skimmer. However, a thick shock structure develops as the jet interacts with the skimmer and the back wall. In figure 7(d) it is clear that the skimmer does not fully penetrate this region and that jet molecules will likely scatter and reheat before being transmitted to the second stage.

It is well-known that complex flow patterns develop when a supersonic jet impinges on a flat plate and spreads radially as a wall jet. In addition to the expected stand-off shock, stagnation bubbles, recirculating flow, and acoustic feedback loops have also been observed [35, 60, 61]. Investigations of large jets impinging on a flat plate in vacuum have shown how the free jet Mach disc evolves into a surface stand-off shock as P_0/P_1 increases [62]. At low P_0/P_1 values, a shock develops at a location close to the expected position of the free jet Mach disc. However, as P_0/P_1 increases, the shock advances less quickly than anticipated and eventually evolves into a stand-off shock

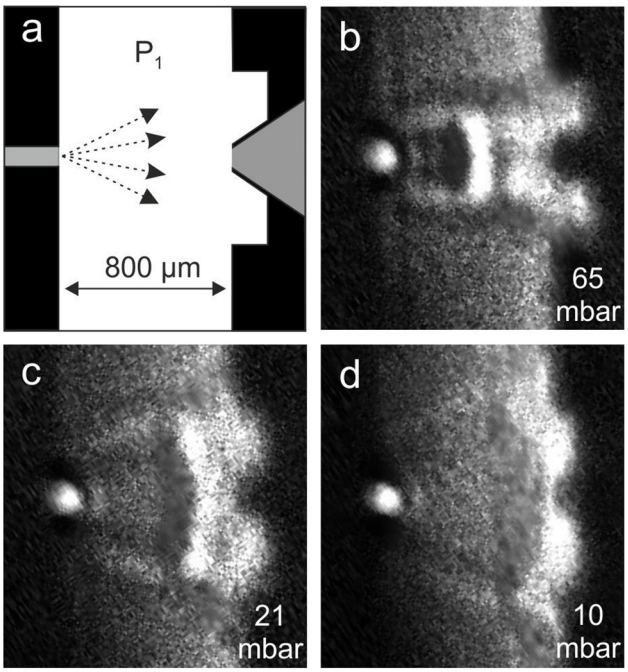

Figure 7. Schlieren imaging of jets interacting with a skimmer. The inlet and skimmer positions are indicated in (a) and images corresponding $P_1 = 65$, 21, and 10 mbar are shown in (b)–(d). $P_0 = 3$ bar. The skimmer is unable to fully penetrate the shock structure.

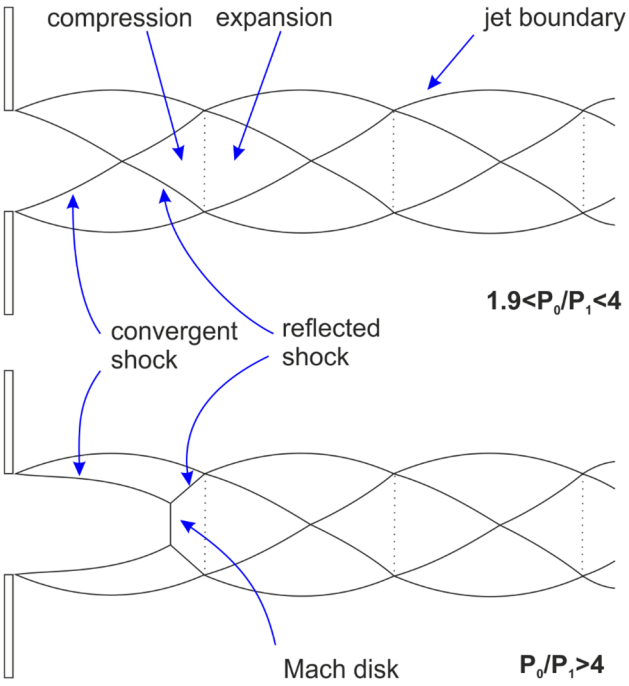

Figure 8. Schematic representations of extended supersonic jets exhibiting multiple shock cells. Reproduced from [63]. © IOP Publishing Ltd. All rights reserved. Reproduced with permission from [64]. JOHN, JAMES E.A.; KEITH, THEO G., GAS DYNAMICS, 3rd, ©2005. Reprinted by permission of Pearson Education, Inc., New York, New York. Reproduced with permission from [65].

whose distance from the surface does not change with further increases in P_0/P_1. The same behavior is observed in figure 7. The jet dimensions appear distorted in figure 7(c) because the Mach disc is further upstream than in a free jet. In figure 7(d),

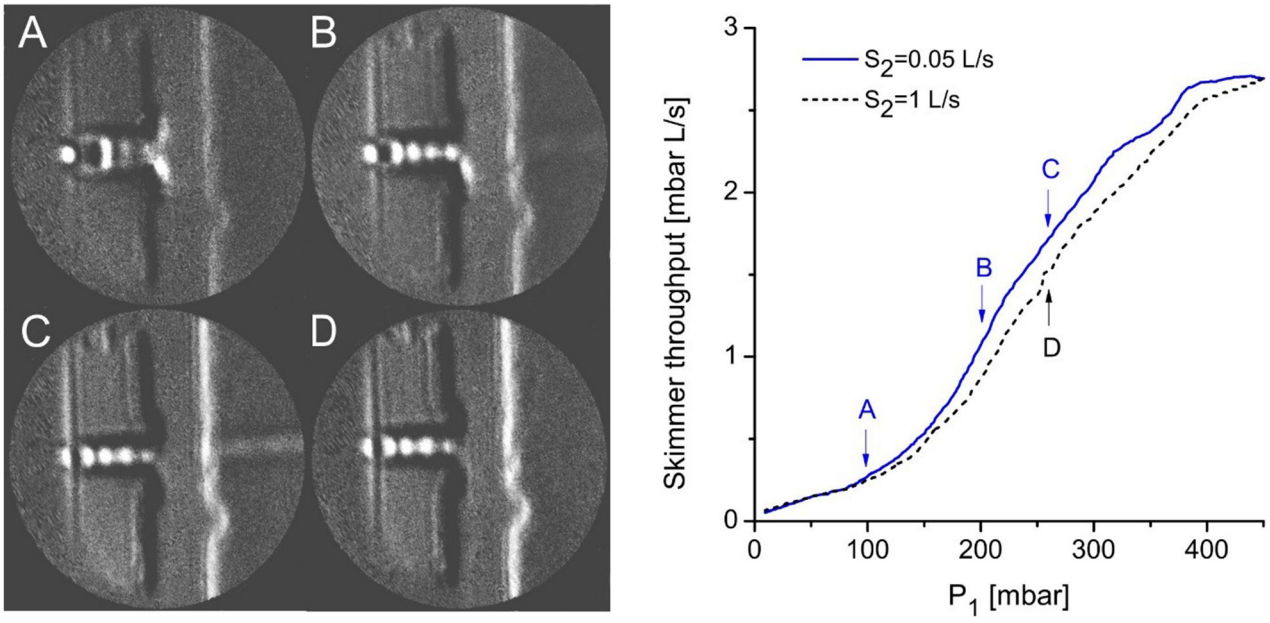

Figure 9. Plots of skimmer throughput against first stage pressure are shown on the right for two different second stage pumping speeds (S_2). Schlieren images corresponding to the indicated points on the curves are shown on the left. The jet formed in the first stage narrows as P_1 increases (A) and (B) and eventually passes through the skimmer where a second expansion yields a collimated beam (C). If the background pressure in the second stage is reduced, the same gas flow passes through the skimmer but a beam cannot be seen (D).

P_1 has been reduced from 21 to 10 mbar but the dark band does not advance further, and may therefore be identified with the fixed separation stand-off shock.

It is clear from figure 7 that more detailed consequences of the pyramidal skimmer geometry are currently masked. The flow patterns at the corners of the square aperture are likely to be complex and further work is required to clarify how this affects the transmitted beam. If necessary, the corners could be moved further away from the centre of the jet by adopting a rectangular pyramidal geometry. The interfering effects of the back wall could be avoided by using a taller skimmer. Unfortunately, extension of the planar fabrication process to substantially thicker wafers is not trivial because of the increased etching time and hard mask thickness required. It may also be advantageous to allow a higher Mach number jet with a thinner Mach disc to develop by increasing the separation between the inlet and the skimmer. However, this would require higher pumping speeds, which is undesirable if the intention is to use MEMS vacuum interfaces in miniature mass spectrometers.

4.3. Expansion into the second stage, and collimated beam production

In molecular beam applications, interest has been focused on the initial supersonic expansion and shock-free sampling from the zone of silence. However, in other fields it has been found that supersonic jets can exhibit an extended periodic structure, representing repeated cycles of over-expansion and re-compression. In jet and rocket propulsion, for example, the bright shock diamonds often seen in exhaust gas are due to ignition of excess fuel in regions where the flow is re-heated. In this section, we describe jet interactions with a skimmer at unusually high first stage pressures and examine how skimmer throughput increases as the Mach disc retracts towards the inlet and the jet develops an extended structure.

It is known that the structure of extended supersonic jets evolves [63–65] as the nozzle pressure ratio increases above the threshold between subsonic and supersonic flow at $P_0/P_1 = 1.9$. Figure 8 shows schematic representations of jets with multiple shock cells, adapted from [63–65]. Gas leaving the nozzle initially over-expands via a rarefaction fan emanating from the rim of the nozzle, but is pushed back towards the jet axis by the ambient gas. For $1.9 < P_0/P_1 < 4$, this process leads to the formation of an axisymmetric, conical shock that converges towards the beam centreline, where it reflects and diverges [63, 66]. When the reflected shock meets the jet boundary, a new rarefaction fan is formed and the cycle begins again. At higher values of P_0/P_1, a Mach disc forms, initially with a small diameter, and the convergent shock reflects from its perimeter rather than the beam centreline.

The graph in figure 9 shows how the gas flow through a 100×100 μm skimmer aperture responds to increasing first stage pressure. The flow was determined by measuring P_2 as the first stage pump was progressively throttled and then multiplying by the known pumping speed. As before, the reservoir pressure was 3 bar. One data set corresponds to pumping of the second stage by a small diaphragm pump with an effective pumping speed of 0.05 l s^{-1}, the other to pumping by a large rotary pump with an effective pumping speed of 1 l s^{-1}. Clearly, the 20-fold difference in the downstream pressure had little impact on the gas flux through the skimmer.

Also shown in figure 9 are schlieren images corresponding to the pressures and pumping arrangements indicated in the graph. The field of view has been expanded compared with figure 7 to show both vacuum stages, separated by the skimmer

die, whose shadow is at the centre. In image A, the barrel shock and Mach disc are clear but a developing downstream shock structure is also evident. The jet appears to narrow and then deflect either side of the skimmer, which is consistent with the gas throughput being low. Retraction of the Mach disc towards the inlet and development of a multiple shock cell structure can be seen in B. The throughput is much higher and a faint beam can now be discerned downstream of the skimmer. The remainder of the jet is deflected only along the lower slope of the skimmer, presumably as a result of slight mis-alignment of the inlet with respect to the skimmer. In C, the jet has narrowed to approximately the size of the skimmer aperture and a collimated beam can clearly be seen in the second stage. This is an unexpected outcome, as transmission of a jet with multiple shock cells does not appear to have been previously considered as a means of producing a molecular beam. D was recorded at the same first stage pressure as C but the second stage pressure was 20× lower due to the use of a bigger pump. There is no indication of a downstream beam even though the throughput was almost the same. These observations suggest that the internal profile of the skimmer is acting as a divergent nozzle. In C, the beam is over-expanded due to the high second stage pressure and consequently contracts and separates from the diverging walls of the skimmer. The beam can be seen in C because contraction of the beam generates strong shock waves that may be visualised by schlieren imaging. It should be noted that the beam diameter in C is approximately 160 μm whereas the skimmer widens to 757 μm. Close inspection of C reveals that the beam is deflected upwards slightly. This is consistent with schlieren imaging of a miniature 2D nozzle, which shows that an over-expanded beam can attach to one side of the divergent section [67]. In D, the much lower second stage pressure allows the beam to fully expand in the nozzle and approach pressure-matched conditions i.e. the beam neither expands nor contracts as it exits the nozzle. In this case, the shock structures and density gradients are weak and the beam cannot be imaged.

In effect, the MEMS vacuum interface described here replicates the function of a single-piece convergent-divergent nozzle but with the tasks of accelerating the gas flow and supersonic expansion being separated by an intermediate free jet. Arguably, the same effect could have been achieved using a convergent-divergent MEMS nozzle [24, 27, 28, 30]. However, the present arrangement has the advantage that beam transmission to the second stage can be modulated remotely at the first stage pump (for example, using a solenoid valve to alter the throttling). Discontinuous vacuum interfaces have been used in miniature ion trap mass spectrometers [68] to reduce the gas load and hence, the size of the vacuum pump.

4.4. Interaction of extended jets with small skimmer apertures

In this section, the increased sensitivity of a smaller skimmer aperture to the periodic structure of the jet is described. To access nozzle pressure ratios up to the point where the beam becomes subsonic ($P_0/P_1 < 1.9$) while at the same time avoiding unsafe pressure differences across the thin skimmer die, the reservoir pressure was reduced from $P_0 = 3$ bar to $P_0 = 1$ bar for these experiments. Figures 10(a) and (b) show representative data for skimmers with 65 × 65 μm and 100 × 100 μm apertures, respectively. For the 65 × 65 μm skimmer, P_2 is not a smooth function of P_1. A weak shoulder at 92 mbar and a series

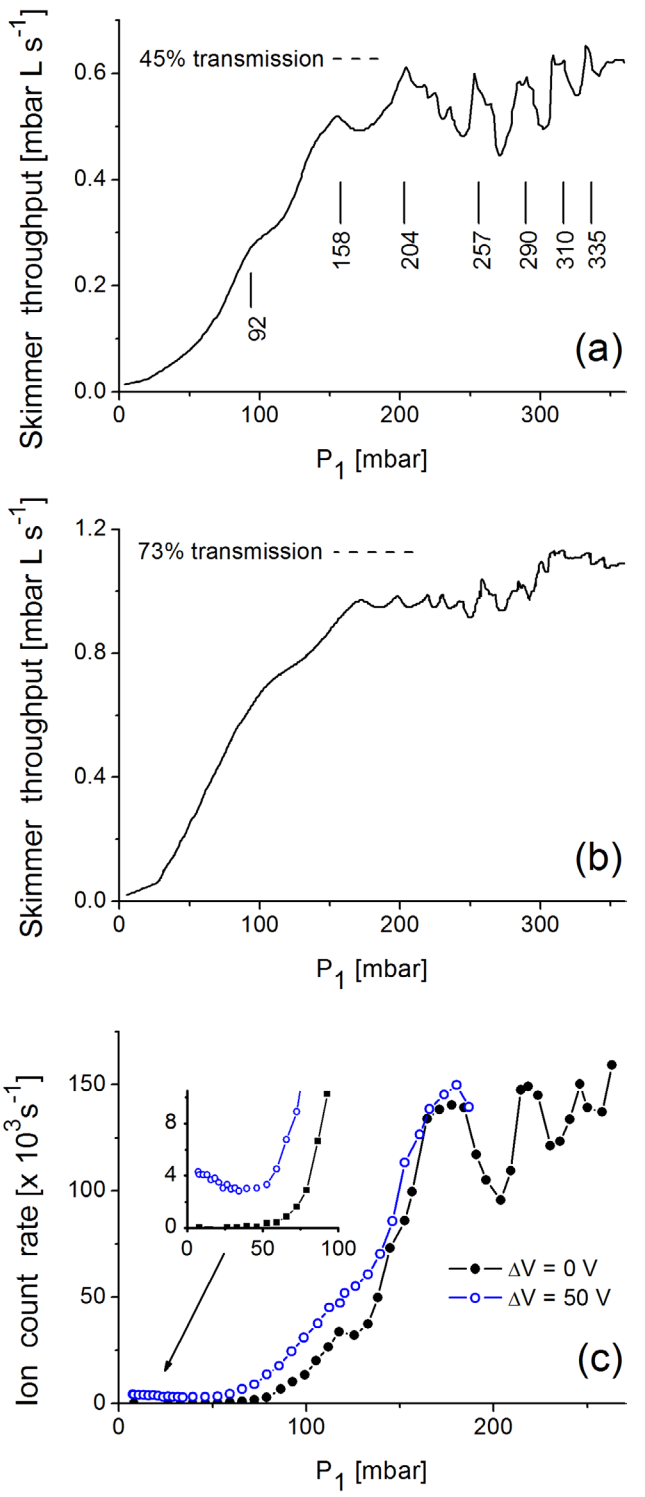

Figure 10. Plots of skimmer throughput against first stage pressure for (a) 65 × 65 μm and (b) 100 × 100 μm apertures with $P_0 = 1$ bar. In (c), the ion flux transmitted through a skimmer used as a mass spectrometer vacuum interface is plotted against first stage pressure. The aperture measured 50 × 50 μm and the bias applied to the inlet with respect to the skimmer is as indicated. Ions were created at $P_0 = 1$ bar.

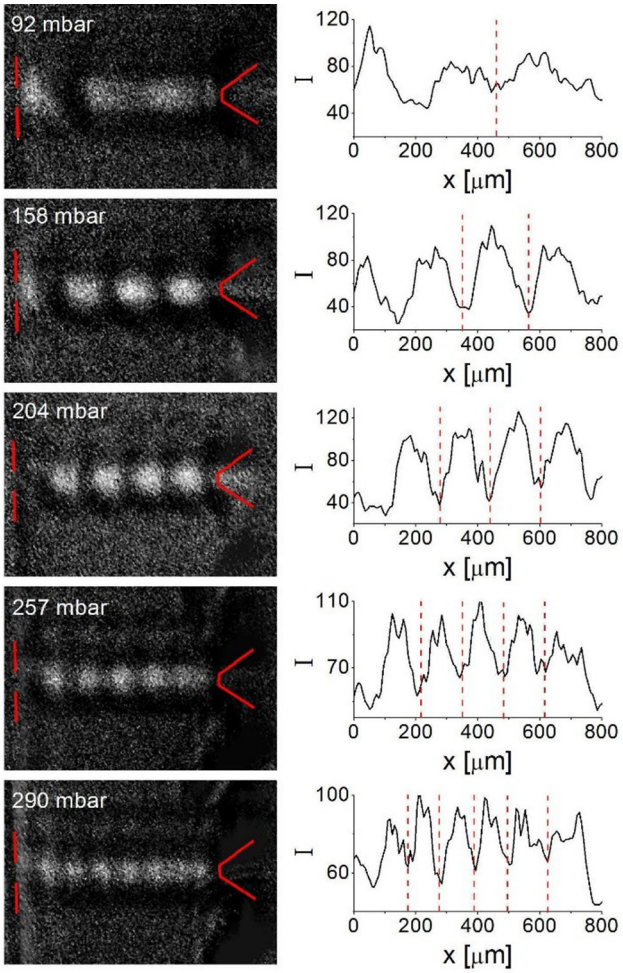

Figure 11. Schlieren images corresponding to the peak positions in figure 10(a). Plots of intensity (I) against position along the beam centreline (x) are shown on the right.

of distinct peaks at 158, 204, 257, 290, 310 and 335 mbar are apparent in the profile. Figure 11 shows a series of schlieren images recorded at first stage pressures corresponding to the first five peaks. The magnification was increased from ×5 to ×8, and only the first vacuum stage was imaged. The definition was improved by subtracting a background image recorded with the jet off and the first stage back-filled with nitrogen via a remote leak valve. Plots of intensity against position along the beam centreline are also shown. At 92 mbar, a developing shock structure comprising two bright maxima beyond the initial expansion is observed with some indication of a weak bow shock directly in front of the skimmer. At 158, 204, and 257 mbar, three, four, and five bright maxima, respectively, are apparent in the images and intensity profiles, with the skimmer location (at 800 μm) corresponding closely to the position of a node in the periodic structure. At 290 mbar, the pattern continues but an elongation and splitting of the final bright maximum, which can also be seen at 257 mbar, is quite pronounced. The splitting may indicate the presence of a bow shock.

To correlate the images in figure 11 with structural features of the supersonic jet, a more detailed schlieren image of a much larger jet was recorded. The MEMS skimmer assembly and inlet capillary were removed and replaced with a tapered pipette tip connected to a nitrogen cylinder. The jet issuing

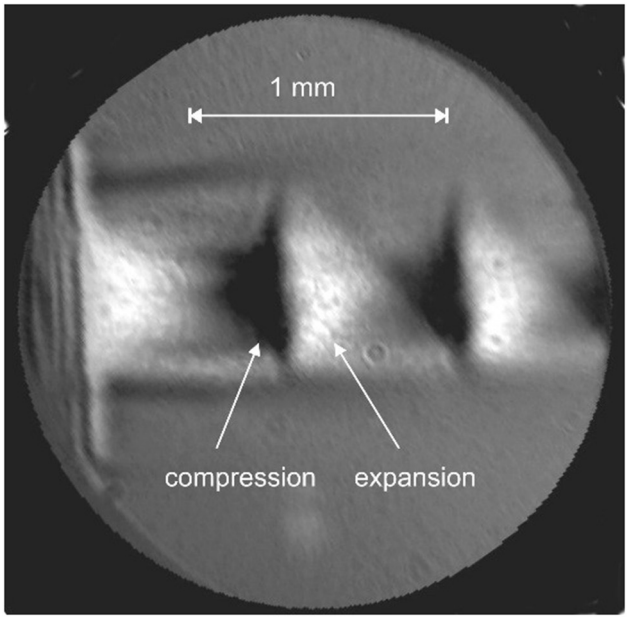

Figure 12. Schlieren image of a supersonic jet from an 800 μm aperture at $P_0/P_1 = 2.75$. Regions of expansion are bright and regions of compression are dark.

from the 800 μm diameter aperture was orientated in the same way as the original jet and allowed to exhaust at atmospheric pressure. Figure 12 shows an image corresponding to $P_0/P_1 = 2.75$. Referring back to figure 8, it is clear that regions of expansion appear as bright areas in the schlieren images and regions of compression are dark.

As the skimmer location corresponds to a dark node in each of the images in figure 11, it can be concluded that enhanced transmission occurs when the skimmer intercepts a region of compression, where the jet boundary and streamlines are pinched inwards and the local number density is high. This interpretation is supported by figure 10(b), which shows that the overall transmission is higher and the peaks are much weaker when the aperture is increased to 100 × 100 μm. Evidently, most of the jet can pass through this wider aperture and subtle differences in the flow dynamics and the diameter of the shock cell structure are of little consequence.

A skimmer with a 50 × 50 μm aperture was used as a vacuum interface for a mass spectrometer as described earlier. Figure 10(c) shows the variation in transmitted ion flux as P_1 was increased. As in figure 10(a), there is a series of distinct peaks. The pumping and pressure measurement arrangements were not the same as in the schlieren imaging apparatus and hence, only approximate correlation between the peak positions is to be expected. The effect of a bias voltage on the inlet is also noteworthy. At $P_1 > 150$ mbar, the bias has no effect, indicating that gas dynamic effects dominate. However, at base pressure, there is a significant increase in the count rate, albeit still to relatively low levels. The initial decline in count rate as the pressure increases to $P_1 = 50$ mbar suggests that the electric field strength (60 kV m^{-1}) is sufficient to drag ions across the shock structure in front of the skimmer but that this effect diminishes as the Mach disc retracts towards the inlet.

For mass spectrometers employing electrospray ionization, the primary requirement of the vacuum interface is to

transmit ions to the second stage ion optics as a collimated beam. As demonstrated in figures 9–11, this can be accomplished by manipulating jets with complex shock structures. While clearly effective for electrospray ionization, the MEMS vacuum interface may not be suited to ion sources requiring shock-free ion transmission. Most important amongst these is the inductively coupled plasma (ICP) source, which generates ions in a high-temperature radio frequency plasma. To avoid ion losses and composition distortion arising from ion-electron recombination and ion-molecule reactions, respectively, collision-free conditions must be maintained downstream of the inlet [13]. Hence, to avoid the high collision rates associated with passage of the flow through shocks, ideal penetration of the zone of silence by the skimmer (figure 1(b)) is desirable for ICP and similar applications.

5. Conclusions

A miniature skimmed free-jet vacuum interface based on a stacked pair of dies incorporating an etched capillary and an electroformed nickel pyramidal skimmer has been demonstrated for the first time, and operated in conjunction with a miniature electrospray mass spectrometer. Sub-millimeter gas jets have been visualised using a schlieren microscope, and the flow field has been followed across two vacuum stages at different pressures.

Unexpectedly, at lower inlet pressure ratios, the jet narrows sufficiently to pass through the skimmer, and a collimated beam is observed in the second vacuum stage. The internal profile of the skimmer appears to act like a divergent nozzle. This has not previously been considered as a mode of operation for a skimmer system. If the skimmer aperture is narrower than the initial supersonic jet, enhanced transmission occurs when the skimmer aperture location coincides with a node in the multiple shock cell structure. At high inlet pressure ratios, the Mach disc is seen to advance towards and then interact with the micro-engineered skimmer. However, it is clear that the gas dynamic characteristics of micro-jets and non-ideal skimmers are more complex than anticipated. So far, there is no evidence of an oblique shock attaching to the rim. In part, this is a result of the Mach disc being relatively thick, which can only be partially explained using the known scaling of shock thickness with mean free path; almost certainly, the effect arises from the known increase in shock thickness at low Reynolds numbers. The most prominent feature of the shock structure is the reflected stand-off shock arising from the close proximity of the back-wall. Erosion of the skimmer cone has also been observed following prolonged use. Further efforts are therefore required to mitigate against these effects, for example by increasing the skimmer height and incorporating additional hard coatings such as titanium. This work is in progress.

Acknowledgments

The authors are extremely grateful to Dr Munir Ahmad for fabricating the experimental silicon dies used in this study.

ORCID iDs

S Wright https://orcid.org/0000-0002-7018-4410
RRA Syms https://orcid.org/0000-0003-0901-8314

References

[1] Miller D R 1988 Free jet sources *Atomic and Molecular Beam Methods* vol 1, ed G Scoles (New York: Oxford University Press) ch 2
[2] Campargue R 1984 Progress in overexpanded supersonic jets and skimmed molecular beams in free-jet zones of silence *J. Phys. Chem.* **88** 4466–74
[3] Jaffe S B and Anderson J B 1969 Molecular beam study of the hydrogen iodide reaction *J. Chem. Phys.* **51** 1057–64
[4] Covey T R, Thomson B A and Schneider B B 2009 Atmospheric pressure ion sources *Mass Spectrom. Rev.* **28** 870–97
[5] Douglas D J and French J B 1988 Gas dynamics of the inductively coupled plasma mass spectrometry interface *J. Anal. At. Spectrom.* **3** 743–7
[6] Fenn J B 2000 Mass spectrometric implications of high-pressure ion sources *Int. J. Mass Spectrom.* **200** 459–78
[7] Malcolm A *et al* 2011 A miniature mass spectrometer for liquid chromatography applications *Rapid Commun. Mass Spectrom.* **25** 3281–8
[8] Wright S *et al* 2015 A microelectromechanical systems-enabled, miniature triple quadrupole mass spectrometer *Anal. Chem.* **87** 3115–22
[9] Wright S, Syms R R A, Moseley R, Hong G, O'Prey S, Boxford W E, Dash N and Edwards P 2010 MEMS-based nanospray-ionization mass spectrometer *J. Microelectromech. Syst.* **19** 1430–43
[10] Syms R R A and Wright S 2016 MEMS mass spectrometers: the next wave of miniaturization *J. Micromech. Microeng.* **26** 023001
[11] Morse M D 1996 Supersonic beam sources *Experimental Methods in the Physical Sciences* vol 29B (New York: Academic) ch 2
[12] Jugroot M, Groth C P T, Thomson B A, Baranov V and Collings B A 2004 Numerical investigation of interface region flows in mass spectrometers: neutral gas transport *J. Phys. D: Appl. Phys.* **37** 1289–300
[13] Farnsworth P B and Spencer R L 2017 Ion sampling and transport in inductively coupled plasma mass spectrometry *Spectrochim. Acta* B **134** 105–22
[14] Kantrowitz A and Grey J 1951 A high intensity source for the molecular beam. Part I. Theoretical *Rev. Sci. Instrum.* **22** 328–32
[15] Ashkenas H and Sherman F S 1966 *Rarefied Gas Dynamics: Proc. 4th Int. Symp. Institude Aerospace Studies (Toronto, 1964)* vol II, ed J H DeLeeuw (New York: Academic) pp 85–105
[16] Gentry W R and Giesse C F 1975 High-precision skimmers for supersonic molecular beams *Rev. Sci. Instrum.* **46** 104
[17] www.beamdynamicsinc.com
[18] Hashimoto Y, Fujisawa T, Morimoto T, Fujita Y, Honma T, Muto S, Noda K, Sato Y and Yamada S 2004 Oxygen gas-sheet beam profile monitor for the synchrotron and storage ring *Nucl. Instrum. Methods Phys. Res.* A **527** 289–300
[19] Subramanian R and Sulkes M 2008 Production of a slit skimmer for use in cold supersonic molecular beams *Rev. Sci. Instrum.* **79** 016101
[20] Tzoganis V, Jeff A and Welsch C P 2014 Gas dynamics considerations in a non-invasive profile monitor for charged particle beams *Vacuum* **109** 417–24

[21] Eder S D, Samelin B, Bracco G, Ansperger K and Holst B 2013 A free jet (supersonic), molecular beam source with automized, 50 nm precision nozzle-skimmer positioning *Rev. Sci. Instrum.* **84** 093303
[22] Shi Q, Chang S-C, Putty M W and Hicks D B 1995 Characterization of electroformed nickel microstructures *Proc. SPIE* **2639** 191–9
[23] Fritz T, Cho H S, Hemker K J, Mokwa W and Schnakenberg U 2002 Characterization of electroplated nickel *Microsyst. Technol.* **9** 87–91
[24] Maurya D K, Das S and Lahiri S K 2005 Silicon MEMS vaporizing liquid microthruster with internal microheater *J. Micromech. Microeng.* **15** 966–70
[25] Lewis D H Jr, Janson S W, Cohen R B and Antonsson E K 2000 Digital micropropulsion *Sensors Actuators* A **80** 143–54
[26] Chaalane A, Chemam R, Houabes M, Yahiaoui R, Metatla A, Ouari B, Metatla N, Mahi D, Dkhissi A and Esteve D 2015 A MEMS-based solid propellant microthruster array for space and military applications *J. Phys: Conf. Ser.* **660** 012137
[27] Bayt R L and Breuer K S 2001 A silicon heat exchanger with integrated intrinsic-point heater demonstrated in a micropropulsion application *Sensors Actuators* A **91** 249–55
[28] London A P, Ayón A A, Epstein A H, Spearing S M, Harrison T, Peles Y and Kerrebrock J L 2001 Microfabrication of a high pressure bipropellant rocket engine *Sensors Actuators* A **92** 351–7
[29] Teasdale D, Milanovic V, Chang P and Pister K S J 2001 Microrockets for smart dust *Smart Mater. Struct.* **10** 1145
[30] Zhang K L, Chou S K, Ang S S and Tang X S 2005 A MEMS-based solid propellant microthruster with Au/Ti igniter *Sensors Actuators* A **122** 113–23
[31] Hao P-F, Ding Y-T, Yao Z-H, He F and Zhou K-Q 2005 Size effect on gas flow in micro nozzles *J. Micromech. Microeng.* **15** 2069–73
[32] Li S, Freidhoff C B, Young R M and Ghodssi R 2003 Fabrication of micronozzles using low-temperature wafer-level bonding with SU-8 *J. Micromech. Microeng.* **13** 732–8
[33] Cai Y, Liu Z and Shi Z 2017 Effects of dimensional size and surface roughness on service performance for a micro Laval nozzle *J. Micromech. Microeng.* **27** 055001
[34] Scroggs S D and Settles G S 1996 An experimental study of supersonic microjets *Exp. Fluids* **21** 401–9
[35] Phalnikar K A, Kumar R and Alvi F S 2008 Experiments on free and impinging supersonic microjets *Exp. Fluids* **44** 819–30
[36] Aniskin V, Mironov S and Maslov A 2013 Investigation of the structure of supersonic nitrogen microjets *Microfluid. Nanofluid.* **14** 605–14
[37] Palmer K, Catalan E V, Lekholm V and Thornell G 2013 Investigation of exhausts from fabricated silicon micronozzles with rectangular and close to rotationally symmetric cross-sections *J. Micromech. Microeng.* **23** 105001
[38] Hong C, Yoshida Y, Matsushita S, Ueno I and Asako Y 2015 Supersonic micro-jet of straight micro-tube exit *J. Therm. Sci. Technol. Japan* **10** 15–00363
[39] Kohle P S and Agrawal A K 2009 Density measurements in a supersonic microjet using miniature rainbow schlieren deflectometry *AIAA J.* **47** 830–8
[40] Huang C, Gregory J W and Sullivan J P 2007 A modified schlieren technique for micro flow visualization *Meas. Sci. Technol.* **18** N32
[41] Braun J, Day P K, Toennies J P, Witte G and Neher E 1997 Micrometer-sized nozzles and skimmers for the production of supersonic He atom beams *Rev. Sci. Instrum.* **68** 3001–9
[42] Lee D B 1969 Anisotropic etching of silicon *J. Appl. Phys.* **40** 4569–74
[43] Bean K 1978 Anisotropic etching of silicon *IEEE Trans. Electron Devices* **25** 1185–93
[44] Bhardwaj J K and Ashraf H 1995 Advanced silicon etching using high-density plasmas *Proc. SPIE* **2639** 224–33
[45] Hynes A M, Ashraf H, Bhardwaj J K, Hopkins J, Johnston I and Shepherd J N 1999 Recent advances in silicon etching for MEMS using the ASE™ process *Sensors Actuators* A **74** 13–17
[46] Freeware (www.astronomie.be/registax/)
[47] Freeware (www.gimp.org/)
[48] Shapiro A H 1953 *The Dynamics and Thermodynamics of Compressible Fluid Flow* vol 2 (New York: Ronald Press)
[49] Liepmann H W and Roshko A 1957 *Elements of Gasdynamics* (New York: Wiley)
[50] Massey B S 1968 *Mechanics of Fluids* (London: Van Nostrand Reinhold)
[51] Murphy H R and Miller D R 1984 Effects of nozzle geometry on kinetics in free-jet expansions *J. Phys. Chem.* **88** 4474–8
[52] Wißdorf W, Müller D, Brachthäuser Y, Langner M, Derpmann V, Klopotowski S, Polaczek C, Kersten H, Brockmann K and Benter T 2016 Gas flow dynamics in inlet capillaries: evidence for non laminar conditions *J. Am. Soc. Mass Spectrom.* **27** 1550–63
[53] Jain V and Lin C X 2006 Numerical modeling of three-dimensional compressible gas flow in microchannels *J. Micromech. Microeng.* **16** 292–302
[54] Bier K and Hagena O 1964 *Rarefied Gas Dynamics: Proc. 4th Int. Symp. Institue Aerospace Studies (Toronto)* vol II, ed J H DeLeeuw (New York: Academic) pp 478–95
[55] Alsmeyer H 1976 Density profiles in argon and nitrogen shock waves measured by the absorption of an electron beam *J. Fluid. Mech.* **74** 497–513
[56] Ramos A, Maté B, Tejeda G, Fernándes J M and Montero S 2000 Raman spectroscopy of hypersonic shock waves *Phys. Rev.* E **62** 4940
[57] Graur I A, Elizarova T G, Ramos A, Tejeda G, Fernández J M and Montero S 2004 A study of shock waves in expanding flows on the basis of spectroscopic experiments and quasi-gasdynamic equations *J. Fluid Mech.* **504** 239–70
[58] Sanna G and Tomassetti G 2005 *Introduction to Molecular Beam Gas Dynamics* (London: Imperial College Press) ch 8
[59] Rothe D E 1970 Experimental study of viscous low-density nozzle flows *NASA Technical Report* CR-116247
[60] Lamont P J and Hunt B L 1980 The impingement of underexpanded, axisymmetric jets on perpendicular and inclined flat plates *J. Fluid Mech.* **100** 471–511
[61] Henderson B 1993 Experiments concerning tones produced by an axisymmetric choked jet impinging on flat plates *J. Sound Vib.* **168** 307–26
[62] Vick R A and Andrews E H 1966 An investigation of highly underexpanded exhaust plumes impinging upon a perpendicular flat surface *NASA Technical Note* D-3269
[63] Buchmann N A, Atkinson C and Soria J 2013 Ultra-high-speed tomographic digital holographic velocimetry in supersonic particle-laden jet flows *Meas. Sci. Technol.* **24** 024005
[64] John J E and Keith T G 2006 *Gas Dynamics* 3rd edn (Englewood Cliffs, NJ: Prentice Hall) ch 14
[65] Norman M L and Winkler K-H A 1985 Supersonic jets *Los Alamos Science* (Berlin: Spring) pp 39–71
[66] Mai C-C and Lin J 2002 Flow structures around an inclined substrate subjected to a supersonic impinging jet in laser cutting *Opt. Laser Technol.* **34** 479–86
[67] Huang C, Gregory J W and Sullivan J P 2007 Flow visualization and pressure measurement in micronozzles *J. Vis.* **10** 281–8
[68] Gao L, Li G, Nie Z, Duncan J, Ouyang Z and Cooks R G 2009 Characterization of a discontinuous atmospheric pressure interface. Multiple ion introduction pulses for improved performance *Int. J. Mass Spectrom.* **283** 30–4